Title

Specialized cells that sense tissue mechanics to regulate Drosophila morphogenesis.

Journal

Developmental Cell, 58(3)

Authors

Ku, Hui-Yu

Harris, Leigh

Bilder, David

Publication Date

2023-02-06

DOI

10.1016/j.devcel.2023.01.004

Peer reviewed

HHS Public Access

Author manuscript

Dev Cell. Author manuscript; available in PMC 2024 August 26.

Published in final edited form as:

Dev Cell. 2023 February 06; 58(3): 211–223.e5. doi:10.1016/j.devcel.2023.01.004.

Specialized cells that sense tissue mechanics to regulate morphogenesis

Hui-Yu Ku[1], **Leigh K. Harris**[1], **David Bilder**[1,2,*]

[1] Department of Molecular and Cell Biology, University of California-Berkeley, Berkeley CA, 94720, USA

[2] Lead contact

SUMMARY

Shaping of developing organs requires dynamic regulation of force and resistance to achieve precise outcomes, but how organs monitor tissue mechanical properties is poorly understood. We show that in developing Drosophila follicles (egg chambers), a single pair of cells performs such monitoring to drive organ shaping. These anterior polar cells secrete a Matrix Metalloproteinase (MMP) which specifies the appropriate degree of tissue elongation, rather than hyper- or hypo-elongated organs. MMP production is negatively regulated by basement membrane (BM) mechanical properties, which are sensed through focal adhesion signaling and autonomous contractile activity; MMP then reciprocally regulates BM remodeling, particularly at the anterior region. Changing BM properties at remote locations alone is sufficient to induce a remodeling response in polar cells. We propose that this small group of cells senses both local and distant stiffness cues to produce factors that pattern the organ's BM mechanics, ensuring proper tissue shape and reproductive success.

INTRODUCTION

Fidelity is a challenge faced by all organisms throughout development. Fidelity in embryonic fate patterning must cope with noise from intrinsically stochastic gene expression, and does so in part by feedback architectures embedded within gene regulatory networks[1–3]. By contrast, fidelity in morphogenesis must cope with tissue mechanical properties that change throughout dynamic growth, monitoring and modifying them to achieve the specific three-dimensional organ shapes necessary to mediate physiology. Feedback through biomechanical means can promote this process, for example in mammalian vasculature where diameters are influenced by the physical properties of lumenal flow[4]. But for many organ types, the regulatory axes underlying morphogenetic precision remain unclear.

* Correspondence: bilder@berkeley.edu.

AUTHOR CONTRIBUTIONS

HK performed the experiments and analyzed the data; LKH designed and executed fibril analysis; HK and DB conceived the research and wrote the manuscript.

DECLARATION OF INTERESTS

The authors declare no competing interests.

Morphogenesis is driven not only by intracellular mechanisms that control actomyosin contractility and cell-cell adhesion, but also extracellular mechanisms that create resistances confronted by cell-generated forces. Growing evidence demonstrates that the basement membrane (BM), a specialized extracellular matrix that is found beneath all epithelia, can actively instruct organ shape, including elongation of the early mammalian embryo and later branching morphogenesis in tubular organs[5–8]. The BM plays biochemical roles to trigger integrin signaling and sequester morphogens and also biophysical roles by creating a specific mechanical environment. This environment, which is sensed by integrin-based focal adhesions, can include stiffness differences that are patterned both spatially and temporally. Such differences are created by regulating the production, distribution, and post-translational modification of BM components, and these patterns can directly dictate tissue shapes. However, an important question remains unanswered: how do developing organs create specific BM patterns and dynamically integrate mechanical information to ensure morphological accuracy?

The fly follicle (egg chamber) is an elegant system to address this question. Each follicle is an organ that gives rise to a single egg that is laid to allow reproduction[9,10]. The follicle has a simple structure (Figure 1A): a layer of somatic cells called the follicle epithelium encases germline tissue in its lumen. The follicle epithelium itself is encased in a BM whose structure and molecular composition are conserved across animal phylogeny. Follicles are first formed as regular spheres, but elongate as they grow during development to produce ellipsoid eggs of a very regular aspect ratio that varies by ± < 4% (Figure 1A and 1B)[11,12]. Proper egg shape is important for reproductive success (see below)[11], and this shape is critically determined by the mechanical properties of the BM underlying the follicle epithelium. As the follicle develops, the BM transitions from being isotropically stiff to form an anterior-posterior (AP) stiffness gradient that peaks in the center. It has been proposed that the degree of egg elongation is specified particularly by the relative stiffness of polar vs central regions of the tissue[13,14].

Here, we describe a mechanism by which BM patterning is actively monitored and modified remotely by a single pair of cells at one end of the follicle. Through focal adhesion-mediated sensing of BM mechanical properties, these cells tune production of a matrix metalloproteinase (MMP) that in turn remodels BM pattern and thus organ shape. Our findings show how a developing tissue can use specialized cells that regulate ECM organization, along with reciprocal communication to these cells via local and distant mechanical sensing, to achieve morphogenetic precision.

RESULTS

Focal adhesions in the PCs restrict follicle elongation

To understand the mechanisms by which ECM can shape tissues, we carried out a genetic screen in which gene products are depleted throughout the follicle epithelium using RNAi transgenes driven by the *traffic jam* driver (*tj-GAL4*). Two hits from this screen, targeting *vinculin* (*vinc*) and *integrin-linked kinase* (*Ilk*), gave a rare phenotype in which follicles are hyperelongated, with aspect ratios that are >10% greater than WT (Figure S1A–S1C and S1F). This phenotype was surprising since both genes encode components of integrin-based

focal adhesions, and depletion of the common β-integrin subunit (Myospheroid, hereafter referred to as Integrin*)* in the follicle epithelium is long known to result in the opposite hypoelongated, 'round egg' phenotype (Figure S1D and S1F)[14,15].

Further investigation revealed that both Vinc and Ilk are highly enriched in polar cells (PCs) compared to the rest of the follicle epithelium (Figure 1A, S1G and S1H). PCs are pairs of cells that segregate early from the follicle epithelium lineage and occupy the anterior and posterior extremes of the follicle[16]. We used genetic mosaics and targeted RNAi to specifically test the role of Vinc in PCs. *vinc* null mitotic clones that include the anterior PCs recapitulated the hyperelongation phenotype, whereas mutant clones that are restricted to the follicle epithelium elongated normally (Figure S1I and S1J). Moreover, *vinc* or *ilk* depletion in PCs alone, using the *upd-GAL4* driver (Figure S2A), also caused hyperelongation (Figure 1C, 1D, 1J, S1E, ans S1F), as did depletion of *integrin* in PCs rather than the follicle epithelium (Figure 1E, 1J, and S1D). By contrast, enhancing integrin signaling by overexpressing either the BM component and integrin ligand Collagen IV (ColIV) (Figure 1F and 1J), or a constitutively active downstream effector of focal adhesion signaling ($RIAM30^{Act}$)[17] (Figure 1G and 1J) in the PCs caused follicle rounding. Coexpression of ColIV failed to shorten hyperelongated follicles induced by PC *vinc* knockdown, while coexpression of $RIAM30^{Act}$ shortened hyperelongated follicles induced by PC *integrin* knockdown (Figure 1H–1J), consistent with a conventional pathway that signals from ECM through integrins. Genotypes producing either rounder or hyperelongated follicles deposited eggs at a much lower rate than controls, indicating that precise follicle dimensions are required for the reproductive fitness of the animal (Figure 1K). Together, these data demonstrate that focal adhesion signaling in PCs is a critical regulator of shape for the entire organ.

Morphogenetic regulation by PC focal adhesions does not involve Upd signaling

PCs are known to secrete the morphogen-like patterning signal Upd to create different cell fates in the follicle, and follicles that receive the wrong dose of this signal fail to elongate appropriately (Figure 2A, 2B, and 2D)[18–20]. This raises the possibility that PC focal adhesion signaling might influence organ shape through changing either Upd levels or the differentiation state of the PCs themselves. To test this possibility, we examined three cell fate markers expressed in WT PCs and the nearby follicle epithelium but found no differences when PC focal adhesion signaling was abrogated (Figure S2B–S2G). The range and level of a STAT activity reporter were also unaffected by manipulating focal adhesion components in the PCs (Figure 2E and S2H–S2K), suggesting normal *upd* production. Finally, epistasis analysis showed that overexpression of *upd* along with *vinc* depletion in the PCs rescued the hyperelongation phenotype caused by *vinc* depletion alone (Figure 2C–2D). These data indicate that focal adhesion signaling within PCs regulates follicle elongation in a parallel, independent path to that governed by Upd.

PC focal adhesion signaling controls follicle BM mechanical properties

To explore alternate mechanisms by which localized focal adhesion signaling could influence the shape of the entire organ, we turned to an assay previously used to assess mechanical properties of the follicle BM. In this 'bursting assay,' organs are placed in a

hypotonic solution, and osmotic pressure leads to swelling and eventually rupture of WT follicles (Figure 3A). The site and rate of mechanical failure under tension in this assay correlate with BM stiffness values measured by indentation atomic force microscopy; for example WT follicles rupture preferentially at either anterior or posterior poles, the softest points in the A-P stiffness gradient (Figure 3B and 3H; Video S1)[13,21]. We compared WT to PC focal adhesion-depleted follicles, as well as previously characterized genotypes that have either softer or stiffer BMs. As expected, removing ColIV in all follicle cells (*tj>ColIV*^{KD}) resulted in rapid bursting with no positional preference, while elevating ColIV fibril secretion by overexpressing EH domain binding protein 1 (EHBP1) in the follicle epithelium (*tj>EHBP1*^{OE})[22] strongly prevented follicle bursting (Figure 3C, 3D and 3H; Video S1). Interestingly, when focal adhesion signaling was reduced in PCs (*upd>vinc*^{KD} or *upd> integrin*^{KD}), follicle bursting was also prevented, nearly altogether (Figure 3E and 3H; Video S1). By contrast, under conditions of PC focal adhesion activation (*upd>RIAM30*^{Act}) the opposite effect was seen: follicles burst rapidly and at sites not restricted to the poles (Figure 3F and 3H; Video S1). We noted that, whereas rupture likelihood in control follicles is evenly divided between the anterior and posterior poles (Figure 3H), burst-resistant genotypes also showed strong reductions in rupture from both poles. These data suggest that focal adhesion signaling in PCs regulates tissue mechanical properties, with increased signaling inducing BM weakening and decreased signaling generating a BM that is more resistant to the stress of expansion.

Altered BM patterning in PC focal adhesion manipulations

We considered mechanisms through which PCs could regulate tissue mechanical properties to control follicle shape. The current ‘molecular corset’ model holds that a developmentally patterned gradient of BM stiffness physically constrains the growing follicle to determine a specific degree of elongation along the A-P axis[23,24]. Since defects in follicle rotation can dysregulate BM organization and therefore organ shape[14], we performed live imaging of follicles cultured *ex vivo*. However, no differences in rotation velocity nor direction were seen when focal adhesion signaling was reduced in PCs (Figure S3A–S3C; Video S2). We used Fluorescence Recovery After Photobleaching (FRAP) of an endogenously GFP-labeled Collagen IV α2 chain (encoded by the Drosophila gene *viking,* hereafter called ColIV-GFP) to assess BM deposition by the follicle. Again, in both mobile fraction and recovery half time, mutants defective in PC focal adhesion signaling did not show significant differences from control (Figure S3D–S3F).

ColIV-GFP in follicles is found in fibrillar as well as non-fibrillar populations; the latter has been proposed to reflect the conventional BM, while the former can confer anisotropic stiffness to it[14,22,25]. Quantitative imaging showed that overall levels of ColIV-GFP were unchanged between WT and PC *vinc*-depleted follicles, suggesting that focal adhesion activities do not affect total BM production (Figure 4A and 4F). However, fibril density in PC *vinc*-depleted follicles was distinctly elevated compared to controls, and individual fibrils had a greater mean length and reduced width (Figure 4A–4C and 4F). This change in BM ‘texture’ was greatest in the anterior but also extended to the posterior. In addition to PC focal adhesion depletion, follicle hyperelongation can be caused by overexpression of the Rab10 effector EHBP1, which increases secretion of fibrillar ColIV[22]. However, PC

vinc-depleted follicles showed a fibril pattern that was different from that seen in EHBP1 overexpression, which causes similar increases in fibril length but only slight localized changes in fibril width and density (Figure S3G and S3H); PC *vinc*-depleted follicles also did not display elevated ColIV secretion (Figure S3I–S3L). Moreover, despite the fact that both genotypes exhibit resistance to bursting, each displayed different dynamic shape changes during hypotonic swelling. PC *vinc*-depleted follicles almost doubled their original size compared to EHBP1-overexpressing follicles, well beyond the extent that WT follicles can swell before bursting (Figure 3I). During swelling, PC focal adhesion-depleted follicles also increased their aspect ratios rapidly, whereas EHBP1-overexpressing follicles, like WT, maintained a constant aspect ratio (Figure 3J). These distinct phenotypes suggest that PCs regulate BM fibril distribution and mechanical properties through a mechanism other than controlling ECM secretion.

MMP1 is the PC focal adhesion effector that specifies tissue elongation

Since PC focal adhesion signaling did not alter the amount of ColIV secreted, we wondered whether it might instead instruct BM patterning through extracellular action. Matrix metalloproteinases (MMPs) can process ECM components extracellularly to adjust stiffness profiles in various contexts. Drosophila has two MMPs, MMP1 and MMP2, that are most closely related to vertebrate MMP19 and MMP11 respectively[26]. Although both fly MMPs are implicated in cell invasion through BMs, overexpression of MMP2 but not MMP1 leads to degradation of ColIV (Figure S4A–S4D) and Perlecan *in vivo*[27], and MMP2 but not MMP1 can degrade Gelatin *ex vivo*[28], suggesting that MMP1 may remodel ECM through other means.

We examined MMP1 in PC *vinc*-depleted follicles and found that MMP1 was enriched solely in the anterior but not the posterior PCs (Figure S4E and S4F). MMP1 signal was stronger when follicles were placed on ice prior to fixation (Figure S4G), perhaps because endocytosis is reduced. In ice preps, increased MMP1 in WT anterior PCs was detected from stages 6 to 8, whereas MMP1 depletion from PCs abolished this signal (Figure 5A–5D and 5H). Mutant follicles in which posterior cell fates are transformed into anterior showed MMP1 at both poles (Figure S4H), confirming that anterior-fated PCs produce MMP1. When analyzed in the ice prep, PC *vinc* depletion caused both increased levels and expanded distribution of MMP1; by contrast elevated PC focal adhesion signaling or local overexpression of ColIV within the PC diminished both level and range of MMP1 (Figure 5E–5H).

Follicles overexpressing MMP1 alone in the PCs showed strong resistance to bursting upon osmotic shock and this manipulation was also sufficient to drive hyperelongation, phenocopying PC focal adhesion depletion (Figure 3H, 5I–J and 5L). Notably, in the bursting assay these follicles expanded their size and aspect ratio with dynamics similar to those of follicles with PC focal adhesion depletion (Figure 3I and 3J; Video S3). They also showed ColIV-GFP fibril profiles that closely resembled PC *vinc*-depleted follicles (Figure 4D and 4F), including increases in fibril density and length that extended into the posterior. Depleting MMP1 from PCs of otherwise WT follicles had the opposite effect: fibril density and length decreased throughout the follicle, and the resultant organs were hypoelongated

and burst quickly (Figure 3G, 3H, 4E, and 4F, and 5L). In functional tests, depleting MMP1 together with focal adhesion components in PCs reversed the hyperelongated phenotype caused by PC focal adhesion depletion alone (Figure 5J–5L). Altogether, these results indicate that MMP1 is a direct downstream effector of focal adhesion signaling in PCs, and is produced to promote BM mechanical properties that encourage organ elongation.

MMP1 expression in PCs is sufficient to cause follicles to hyperelongate and resist bursting upon osmotic challenge. Since these phenotypes are suggestive of an activity other than canonical ECM degradation, we compared the effects of MMP1 and MMP2 on transgenically-expressed ColIV-GFP. When produced in PCs of otherwise WT follicles (*upd>ColIV-GFP*^{OE}), ColIV-GFP incorporation could be detected 45 um from the anterior pole (Figure S4I and S4N). When MMP2 was co-expressed in PCs from these follicles, almost no ColIV-GFP could be detected and the follicle rounding caused by ColIV-GFP overexpression was suppressed (Figure S4J, S4M, and S4N). These phenotypes are consistent with MMP2 digesting the transgenic protein. By contrast, when MMP1 was co-expressed with ColIV-GFP in PCs, follicles hyperelongated as expected, and the range of ColIV-GFP diffusion was intermediate between WT and MMP2 overexpression (Figure S4K–S4N), possibly because of enhanced local incorporation. These results suggest that MMP1 from PCs does not degrade the BM; instead, it may process substrates that alter BM mechanics.

Hyperelongation in MMP1-overexpressing follicles could occur through equivalent mechanical changes to all regions of the organ, or it could reflect localized changes for instance at one pole. Neither *ex vivo* or *in vivo* culture conditions currently allow live monitoring of long-term follicle elongation. We photobleached squares of ColIV-GFP at different regions of follicles and assessed the changes in these fiduciary marks following osmotic swelling, prior to bursting (Figure 3K). In control follicles, relative dimensions of photobleached areas in the anterior, central and posterior follicle were unchanged, indicating that regions expand isotropically (Figure 3L). Isotropic expansion in these regions was also seen in follicles that were hyperelongated due to EHBP1 overexpression (Figure 3L). By contrast, in hyperelongated *PC>MMP1*-overexpressing or *PC>vinc*-depleted follicles, the photobleached region at the anterior region showed increased expansion along the AP axis, becoming ~30% more rectangular (Figure 3L). A lower but significant degree of AP expansion was seen in central, and, for *PC>vinc*-depletion, posterior bleached regions of these follicles. This result suggests that PC focal adhesion signaling regulates most strongly the mechanical properties of the anterior follicle, the area in which the greatest impact on ColIV patterning are also seen.

PCs perceive and respond to distant mechanical cues through focal adhesion signaling

Data above indicate that PC MMP1 plays a pivotal role in governing follicle elongation, and that its activity levels are tuned by autonomous focal adhesion signaling. Quantitative imaging shows that PC MMP1 can lead to modification of BM texture at a significant distance as well as locally. We wondered if such long-range regulation was reciprocal, and whether the PCs could sense and react to remote changes in the BM as well.

To test this possibility, we used the *mirror* driver (*mirr-GAL4*) to alter BM in a central follicle region that is 6–8 cell widths (>60μm) away from the PCs (Figure S4A). Bursting assays suggested that this change is limited locally, since manipulated follicles still burst at lateral or polar regions (Figure 6A; Video S3). Remarkably, either elevating ColIV production (*mirr>ColIV*^{OE}) or fibril secretion (*mirr>EHBP1*^{OE}) in this central region was sufficient to induce MMP1 production in the anterior PC (Figure 6B and 6C), while depleting ColIV in this region (*mirr>ColIV*^{KD}) had the opposite impact (Figure 6D). We found that a follicle with reduced central BM that also has defective focal adhesion signaling in PCs still elevates MMP1 protein, while the same BM manipulation in a follicle that has defective focal adhesion signaling in follicle epithelium but not PCs failed to do so (Figure 6E and 6F). Thus, sensing of distant BM mechanics, like sensing of local BM mechanics, is mediated by focal adhesion signaling within the PCs.

We considered whether other PC activities might be involved in the response. However, Upd production and signaling range were comparable in control and centrally-manipulated follicles (Figure S5A–S5C), and depleting *α-catenin* in PCs caused neither follicle elongation defects nor changes in MMP1 production (Figure S5D–S5I), arguing against input from cell-cell adhesive changes with neighboring follicle epithelial cells. In summary, these data unexpectedly reveal that PCs use focal adhesions to perceive mechanical cues not just from local BM but also from distant sites in the organ, and respond by adjusting MMP1 production accordingly.

BM sensing relies on contractility of the PC

How could PCs perceive local and distant mechanical cues? Interestingly, live imaging of PCs revealed intriguing apicobasal pulsatile contractility (Figure 7A; Video S4) that was not seen in neighboring FCs. Contractility was seen only in anterior and not posterior FCs, and initiated following st. 6 (Figure 7A; Video S4). Following collagenase treatment, PCs showed stronger retraction away from the digested BM compared to the neighboring follicle epithelium (Figure 7B–7D), raising the possibility that PCs are under higher tension. This was confirmed by comparing recoil velocities when lateral PC or follicle epithelial cell cortices were severed by a laser (Figure 7E). The results suggested that PCs might actively tug on the BM to assess its physical properties.

To explore whether distant BM properties could influence contractile frequency, we assessed PC dynamics in *mirr>EHBP1*^{OE} follicles. Indeed, the frequency of oscillation was modestly but significantly increased (Figure 7F and 7G; Video S5). Similar changes were observed in follicles with reduced focal adhesion signaling in PCs (*upd>vinc*^{KD}), while oscillations were decreased when focal adhesion signaling was activated (*upd>RIAM30*^{ACT}) (Figure 7F and 7G; Video S5), consistent with a hypothesis that contractility scales with stiffness sensed by PCs. Remarkably, enhancing PC contractile frequency by depleting myosin phosphatase activity (*upd>myosin binding subunit (mbs)*^{KD})[29] was sufficient to induce hyperelongation of the follicle along with MMP1 upregulation, while reducing it by depleting the myosin heavy chain (*upd>zipper*^{KD}) had the opposite effect (Figure 7F–7J; Video S5). Taken together, these data suggest that PCs can sense and modulate organ-wide BM properties through focal adhesion-linked contractility.

DISCUSSION

It is now appreciated that anisotropic ECM organization can drive tissue shape in both vertebrates and invertebrates, playing critical roles from early embryos to developing organs to adult reproduction. Yet how specifically patterned BMs are generated and maintained is poorly understood. This work provides a model for how specialized cells can specify local and long-range mechanical properties including by regulating BM texture. Our data suggest that as elongation of the Drosophila follicle initiates, PCs at the anterior pole use focal adhesion signaling to perceive an initial low degree of graded BM stiffness, and then tune MMP1 activity to promote formation of BM fibrils that can confer anisotropic tensile strength. This process must be carefully regulated to ensure that it does not result in hyperelongation. Interestingly, the BM also provides reciprocal biomechanical feedback to regulate the PCs. As the follicle stiffens, PCs experience more focal adhesion signaling which then moderates MMP production. These mechanical monitoring and modifying processes encompass not just the local anterior environment but extend more broadly through the tissue. Indeed, a striking finding of this work is that BM changes in the follicle center are sensed at a distance by focal adhesion signaling restricted to the PC, although we remain ignorant of how these changes are transmitted. Overall, our work uncovers a mechanism by which a growing organ morphogenetically self-organizes, dynamically regulating its own BM patterning to ensure appropriate shape.

The effector molecule through which PCs specify non-autonomous BM organization is the fly matrix metalloprotease MMP1. When PC MMP1 levels increase, ColIV fibril density increases, the BM becomes more resistant to mechanical failure during expansion, and tissue elongation along the A-P axis increases; the opposite occurs when PC MMP1 levels are experimentally reduced. This unexpected result is contradictory to the canonical ECM-degrading role of MMPs. However, it is consistent with recent studies and earlier work establishing that BM Collagen IV in developing organs is highly dynamic and its remodeling can be promoted by activity of MMP1 and other metalloproteinases[30–32]. In all of these cases, the direct mechanism of Collagen IV regulation has not been discerned. Our data show that MMP1 does not control overall ColIV levels; moreover, MMP1 is unlikely to promote formation of *de novo* BM fibrils that are organized prior to secretion[22]. Instead, they suggest that MMP1 activity results in altered extracellular organization of ColIV, specifically promoting remodeling from the conventional isotropic basal lamina into a fibril network whose characteristics include increased density. The impact of MMP1 on mechanical properties is most strong at the anterior but ramifies further into the organ. The difference between MMP1's limited anterior range and its long-range impact on ColIV organization suggests that MMP1's effects are indirect, perhaps by proteolytically regulating an unknown factor. Through this or another mechanism, PC-produced MMP1 fashions a BM framework whose specific texture drives appropriate elongation of the entire organ, enhancing reproductive fitness for the organism.

Current data do not allow us to define the specific mechanical property of the BM that MMP1 activity promotes. Atomic force microscopy of follicle BM has demonstrated that apparent elastic modulus assessed by probe indentation negatively correlates with the axis of increased elongation during growth and sites where tissue rupture is most likely

to occur under osmotic pressure[13,21,25,33]. Yet this stiffness measured perpendicular to the BM plane seems unlikely to be the only property associated with the ability of the matrix to accommodate organ expansion. The striking increase in aspect ratio of MMP1-overexpressing follicles during osmotic swelling hints that MMP1 promotes enhanced amenability to tissue expansion without rupture. On the other hand, we find that MMP1 also promotes the anterior narrowing that makes st. 8 follicles distinctly 'pointy', both during development and in the osmotic swelling assay (Figure S6). This contribution seems inconsistent with a simple role for MMP1 in increasing BM pliability, and highlights the knowledge gap between specific spatial organizations of ECM and their observed biomechanical properties.

Our findings point to an unappreciated role of the two anterior PCs as specialized regulators of tissue mechanics. Live imaging demonstrates that these PCs are highly contractile, repeatedly tugging on the follicle BM, in contrast to the non-contractile neighboring epithelium (in which mechanosensitive Vinculin plays no apparent role). Moreover, PC contractility increases with distant elevation of BM ColIV levels, consistent with a model in which PCs use focal adhesion sensing to assess the tissue rigidity landscape. That both static and migrating cells can sample substrate stiffness via cellular contractility is well-established[34]. Moreover, in several cancer cell lines, ECM composition has been found to regulate MMP activity, which may promote tumor cell invasion during pathology[35–39]. Our work identifies a physiological role for this signaling axis in sensing the global mechanical landscape during normal development, and then using the information to non-autonomously regulate BM patterning. It is interesting to note that the BM patterning role of PCs, mediated by MMP1 production, works in parallel to their Upd-mediated cell fate patterning role; indeed, ectopic PCs induced in the follicle epithelium are also contractile, produce MMP1, and promote ectopic pole-like bursting in the swelling assay (Figure S7; Videos S6). Such sufficiency as well as necessity data underscore how a few such specialized cells can be critical architects that shape the tissue mechanical environment.

LIMITATIONS OF THE STUDY

As discussed above, although this study provides evidence that PCs can sense distant as well as local changes in BM properties, the mechanism by which they do so remains unknown. Our data also do not reveal the direct effector that alters BM texture and mechanics in response to MMP1 activity provided by the PCs. Finally, while the swelling assay provides valuable information about tissue material properties, we have not directly measured BM stiffness in this study using AFM or related techniques. A full understanding of how the follicle uses the mechanisms described to ensure appropriate egg shape will be the subject of future work.

STAR★METHODS

Resource availability

Lead contact

- Further information and requests for resources and reagents should be directed to and will be fulfilled by the lead contact, David Bilder (bilder@berkeley.edu).

Materials availability

- This study did not generate new reagents.

Data and code availability

- Data reported in this paper will be shared by the lead contact upon request.
- This paper does not report original code. All code used in MATLAB analysis procedure and the code implementing the calculations is available from the lead contact upon request.
- Any additional information required to reanalyze the data reported in this work paper is available from the Lead Contact upon request.

Experimental model and subject details

Drosophila stock, husbandry, housing, and rearing condition—See Table S1 and Key resource table for detailed strains and genotypes of the experimental animals. Flies were kept on cornmeal molasses food in 28.5 ×95 mm vials at 25°C unless indicated otherwise, with dried yeast added to increase fecundity. Experimental crosses were kept at 25°C. For *GAL4*/*GAL80*^{TS} experiments, animals were kept at 25 °C until third instar (L3), then transferred to 18°C before eclosion. Newly eclosed adults were collected within 48 hours, followed by shifting to 30 °C to allow expression of transgenes. For clonal induction via heat-shock-induced flippase, animals were heat-shocked at L3 at 37°C for 13 minutes (flip-out clones) or 1 hour (mitotic clones) and then returned to 25°C for seven days before ovary dissection. For experiments that combine clonal induction and *GAL4*/*GAL80*^{TS} (i.e., *vinc*$^{102.1}$; *mirr*^{TS}>*ColIV*^{KD}), animals were kept at 18°C before eclosion except for heat-shock at L3. The eclosed adults were then transferred to 30°C for one day before dissection.

Methods details

Oviposition—Ten females and five males were kept in cages on apple juice plates and yeast paste at 30 °C. Deposited eggs were collected in fixed time windows (25°C: 22 hours; 30°C: 18 hours) using paintbrush and nylon mesh, then rinsed with ddH_2O and dried with tissue paper. Egg numbers were determined by the total weight divided by weight of single egg. Numbers of eggs laid from one female fly were quantified; mean value from different control experiments was defined as 100%. The assays were repeated four times independently.

Immunofluorescence Staining—Antibodies, reagents, and working concentrations used are listed in Key resource table. In brief, adult ovary dissections were performed in Schneider's medium, followed by fixation in 4% paraformaldehyde (PFA) for 15 minutes. After being washed with PBS three times, the samples were incubated in staining solution (5% normal goat serum in PBS) with primary antibodies. Following three more washes with PBS, samples were incubated with secondary antibodies in staining solution and washed before being mounting in antifade. Most antibody staining was carried out either at room temperature for 3 hours or at 4°C overnight. Anti-GFP nanobody used to visualize extracellular ColIV-GFP was performed at room temperature for 15 minutes. For MMP1 stains, follicles were kept in culture medium on ice for 2 hours prior to fixation, except for Figs. 6B–6C and S4E–F, which were performed without ice treatment. Solutions were prepared with 0.2% Triton X-100 except when staining extracellular ColIV. For collagenase treatment, dissected follicles were incubated in collagenase (1000 U/mL in Schneider's medium) for 30–45 minutes at room temperature, followed by three washes with medium, one brief rinse with PBS, and then subjected to fixation and antibody staining. Most images were acquired using a Zeiss LSM 700 microscope with a 20x (Plan Apochromat 20x/NA 0.8) or a 40x (LD C-Apochromat 40x/NA 1.1 W Korr M27) objective. For detailed ColIV-GFP pattern analysis, a Zeiss LSM 780 microscope was used with a 40x (LD C-Apochromat 40x/NA 1.2 W Korr M27) objective. Pinhole settings ranged from 1 to 1.8 Airy units.

Bursting Assay—Follicles dissected from the muscle sheath were transferred to PBS and then placed onto poly-D lysine-coated glass-bottom dishes (MetTek). 1:10 serial dilutions of PBS with sterilized H_2O were performed three times. The follicle swelling process was acquired with a 10x objective (Zeiss, Plan-Neofluar 10x/0.30 M27) every 15 seconds for 45 minutes. Time-lapse brightfield images were post-processed using FIJI to determine swelling dynamics. Brightfield images were thresholded to extract sample outlines, and then converted to binary followed by the fill holes function. The watershed was applied at the final step to separate follicles from stalk and generate individual masks. Area and aspect ratio measurements were retrieved using analyze particle function with size exclusion. Values of individual data point (T_i) were subtracted from respective initial time points (T_0) before being normalized to T_0. Plots showing mean ± standard deviation were generated by Prism.

Ex vivo Culture and Live Imaging—Follicles were cultured *ex vivo* as previously described[14]; the osmolality of Schneider's medium was adjusted to 260 Osm/L. Time-lapse images were acquired at 22–23°C at stage 6 and 8 follicles (staged by measuring nurse cell nuclear diameter and the accumulation of yolk) using an inverted confocal microscope (Zeiss LSM 700) equipped with a 40x objective (LD C-Apochromat 40x/NA 1.1 W Korr M27). To determine follicle epithelium rotation velocity, z-stack images of Histone2Av-GFP were acquired for 57–65 focal planes separated by 0.7 μm (total of 40–45 μm) every 4 minutes for 1 hour. Trajectories of individual follicle epithelium nuclei were traced using iMaris. For the FRAP assay on ColIV-GFP, the center of the follicle BM was digitally zoomed at 4.0, z-stacks of 10 planes separated by 0.47 μm were acquired every 10 seconds (pre-bleach) for 1 minute followed by every 2 minutes (post-bleach) for 2 hours. Bleaching used a 488 nm laser set to 100% power (10 mW, two iterations), with differential z locked

to the plane of the BM. The bleached region equals 26–27 μm^2. Post-processing images to determine ColIV-GFP recovery, protein half-life, and mobility fractions were obtained through FIJI and plot in Prism. The same bleached condition was applied in the BM anisotropy assay during swelling, except the region was 10×10 μm^2. Regions were chosen in anterior, middle, and posterior through equal division of the A-P axis into three parts, and the center of each part was bleached. Aspect ratio of the bleached region before and after swelling was quantified by measuring the bleached curvature length in cross sections in Zen. To visualize PCs or follicle epithelium contractility, Fas3-GFP transgenic stocks or CellMask staining (Deep Red, 1000x dilution) were used respectively. PCs or follicle epithelium were imaged with a digital zoom set for 4.0 with a single plane acquired every 1-second (stage 8) or 2 seconds (stage 6). To prevent photobleaching, both pixel dwell (3.15 μs) and laser power (1.5%) were minimized. Images were first processed through FIJI to quantify the area of all data points for individual experiments, followed by importing to Matlab to retrieve the frequency of cell contractility.

Laser Ablation—Stage 8 follicles carrying Indy-GFP or Fas3-GFP were mounted in culture medium on a two-photon laser microscope (Zeiss LSM 980 NLO, controlled by ZEN 3.3 Blue) with a C-Apochromat 40x/1.2 W Korr objective. Single plane image acquisition was carried out through crop area function set to 21.2x with bidirectional scanning mode, and a region of 10×10 μm^2 was collected for a frame time of 93.08 ms. Images were acquired using GaAsP-PMT detector. Lateral membrane cuts were achieved through a circular ROI diameter of 0.5 μm at 800nm (100% power, source between 1.2–1.3 W) with the same scanning speed. Recordings used 397 ms between-frame intervals. To determine recoil velocity, vertices of apical and basal displacement in post-ablation frames were manually tracked using Fiji. Data statistics and plotting were performed in Prism.

Image Post Processing and Data Analyses

Quantifying follicle shape: For aspect ratio (AR) measurement, lengths along AP and DV axes were determined manually in either Zen black (imaging-processing mode) or in FIJI. Curvature ratio (pointiness) of the follicle was determined by identifying the ratio between the radii of best-fit circles in anterior (Ra) or posterior (Rp) pole, modified from[40]. Correlation between elongation (AR) and curvature ratio (Rp/Ra) of different follicle genotypes were plotted in Prism to retrieve R square[41]. Curvature changes in the swelling assay were quantified by calculating ratios of final time point to initial time point for each follicle.

Follicle epithelium migration: Time-lapse stack images of follicles with His2Av-GFP were analyzed using Imaris 9.2.1 (Bitplane, Oxford Instruments). Trajectories of follicle epithelium cells were obtained through a spot-tracking module. The estimated diameters of spot for follicle epithelium nuclei in xy and z were 3 μm with model PSF elongate along the z-axis. Quality filter was defined from 5–25. The autoregressive motion algorithm was applied with a maximum distance of 3.54 μm for two consecutive time points. Trajectories from tracking duration less than 10 minutes and from nurse cells were excluded for following analysis. The follicle epithelium trajectories were further grouped according to the mean velocity ranging from 0–0.2, 0.2–3, 0.3–0.4, 0.4–0.5, and 0.5–0.6 μm•min^{-1}.

Three-dimensional surpass images in orthogonal view were shown with spots at the final time point tailed by trajectories color-coded according to the respective velocity group. Data were plotted and analyzed in Prism.

FRAP on ColIV-GFP: Times series of a single focal plane were analyzed, with drifted images excluded. Pixel intensities of three ROIs (region of interest) were extracted from FIJI as follows: (1) BL: region bleached by 488 laser, (2) BG: background without any target fluorescence, and (3) REF: un-bleached region with targeted fluorescence. Corrections followed by curve fitting (exponential recovery) were performed to retrieve recovery rate and mobile fraction as previously described[42]. Plotting of data and statistics methods were perform in Prism.

PCs contractility Dynamics: Fas3-GFP confocal images were first processed in FIJI with a procedure similar to that described in the bursting assay to obtain area in the control and mutant PCs overtime. Raw time-lapse images went through bleach correction via histogram matching before mask thresholding. For individual sample (i) at the time point (j), differences between area (A_{ij}) to respective mean ($A_{avg.i}$) were calculated before normalized with a respective mean ($A_{avg.i}$). Quantifications for dynamic contractility were subsequently determined using MATLAB (R2021a, MathWorks) with a customized script. Raw signals were smoothed through a Savitzky–Golay filter of polynomial order 3 to data frames of length 61. The fitted curve was further used for high- and low-peak identification. For individual sample, cycling time was determined by mean intervals between peaks and subsequent converted for respective frequency. Finally, statistical analysis of PC contractility frequency in the control and mutants was performed and plotted in Prism.

ColIV Pattern and Fibril Segmentation: Confocal images of ColIV-GFP fibrils were analyzed using custom MATLAB code. Briefly, a Frangi filter was used to calculate the likelihood of a given region being part of a vessel-like or ridge-like structure, and this likelihood was used to segment individual fibrils. This enabled accurate detection and analysis of fibrils of different sizes and fluorescence intensities.

Images were first smoothed using a Gaussian filter with a sigma of 2 pixels (1 pixel = 51.9 nm) and filter size of 3 pixels. The blurred image was then analyzed using a Hessian-based Frangi Vesselness filter (Dirk-Jan Kroon, 2021. https://www.mathworks.com/matlabcentral/fileexchange/24409-hessian-based-frangi-vesselness-filter. Retrieved March 1, 2021). Sigma values from 1 to 16 pixels were iterated over, incrementing by a step size of 1 pixel. This analysis yielded two output images that were used for further analysis: a vessel-enhanced image where each pixel value reflects the maximum likelihood that there is a vessel or ridge structure present, and a scale image that records the vessel width that resulted in the maximum likelihood. An adaptive threshold was applied to the vessel-enhanced image with a neighborhood size of 31×31 pixels to segment fibrils. The thresholded image was masked by the overall follicle outline. This overall outline was determined using the multithresh function to find 7 threshold values using Otsu's method. The blurred follicle image was thresholded using the lowest value, holes were filled, and the outline was eroded using a disk of radius 40 pixels. Small objects under 100 pixels in area were also removed.

At this point, the region props function was then used to analyze individual segmented fibrils. Fibrils with a mean fluorescence intensity below the second lowest of the 7 thresholds calculated above were removed. Fibril length was determined by fitting each segmented fibril with an ellipse and taking the major axis. Fibril width used the average scale image output from the Frangi vesselness filter. Fibril density was calculated by skeletonizing all segmented fibrils and dividing the number of fibril backbone pixels by the total follicle pixel area. Analysis along the A-P axis was performed by dividing the follicle into 5 equally sized regions. Fibrils were assigned to each region according to their centroid position, and the average fibril width and length was calculated for each region. Fibril density was calculated for the entire region at once using the skeletonized fibril image and follicle outline. These per-follicle averages were then analyzed in Figure 3, with the statistics and error bars reflecting the differences between follicles of a given genotype.

Quantification and statistical analysis

Statistics and reproducibility—For control and mutant follicle analysis, adult females ovaries were collected from greater than 6 animals of independent experiments. No data sets were excluded from fixed samples. For bursting assays, samples with erroneous angles over time were not included in area and AR dynamic analysis. Drifting of *ex vivo* cultured follicle was terminated immediately in live imaging. Images and video presented are representative of data sets. The numbers for each individual experiment and the statistical method performed (via GraphPad software: Prism) are indicated in the legends and summarized as follows: Dunnett's multiple comparisons for Fig. 1J, 2D, 5K, and 7J. One-way ANOVA for S1F, S4M-S4N, and S6D. Multiple t test for Fig. 3L, 4F, S2K, S3C, S3H, and S5C. Unpaired Mann-Whitney test for S5F and Fig. 7D–7E. Linear regression for S6A-S6C. Kolmogorov-Smirnov (KS) test for Fig. 7G, S3E–S3F, and S3L. Predetermination of sample size using statistical methods was not performed. Experiments were not randomized; investigators were not blinded when conducting experiments and analyzing results.

Supplementary Material

Refer to Web version on PubMed Central for supplementary material.

ACKNOWLEDGEMENTS

We thank Nick Brown, Trudi Schupbach, Stéphane Noselli, Duojia Pan, Guy Tanentzapf, and the Bloomington, Vienna and Kyoto stock centers for fly strains. We also thank DSHB for antibodies, Hernan Garcia for use of the Zeiss 780 microscope, Holly Aaron and Feather Ives (CRL Molecular Imaging Center, RRID:SCR_017852) for Imaris and technical support, and Daniel Fletcher and Bilder lab members for helpful discussions. This work was funded by NIH R35 GM130388 to DB and a Helen Hay Whitney postdoctoral fellowship to LKH.

INCLUSION AND DIVERSITY

We support inclusive, diverse, and equitable conduct of research.

REFERENCES

1. Dubuis JO, Samanta R, and Gregor T (2013). Accurate measurements of dynamics and reproducibility in small genetic networks. Molecular Systems Biology 9, 639. 10.1038/msb.2012.72. [PubMed: 23340845]
2. Exelby K, Herrera-Delgado E, Perez LG, Perez-Carrasco R, Sagner A, Metzis V, Sollich P, and Briscoe J (2021). Precision of tissue patterning is controlled by dynamical properties of gene regulatory networks. Development 148. 10.1242/dev.197566.
3. Petkova MD, Tkačik G, Bialek W, Wieschaus EF, and Gregor T (2019). Optimal Decoding of Cellular Identities in a Genetic Network. Cell 176, 844–855.e815. 10.1016/j.cell.2019.01.007. [PubMed: 30712870]
4. Humphrey JD, and Schwartz MA (2021). Vascular Mechanobiology: Homeostasis, Adaptation, and Disease. Annu Rev Biomed Eng 23, 1–27 10.1146/annurev-bioeng-092419-. [PubMed: 34255994]
5. Sekiguchi R, and Yamada KM (2018). Basement Membranes in Development and Disease. Curr Top Dev Biol 130, 143–191. 10.1016/bs.ctdb.2018.02.005. [PubMed: 29853176]
6. Kyprianou C, Christodoulou N, Hamilton RS, Nahaboo W, Boomgaard DS, Amadei G, Migeotte I, and Zernicka-Goetz M (2020). Basement membrane remodelling regulates mouse embryogenesis. Nature 582, 253–258. 10.1038/s41586-020-2264-2. [PubMed: 32523119]
7. Khalilgharibi N, and Mao Y (2021). To form and function: on the role of basement membrane mechanics in tissue development, homeostasis and disease. Open Biology 11. 10.1098/rsob.200360.
8. Sherwood DR (2021). Basement membrane remodeling guides cell migration and cell morphogenesis during development. Current Opinion in Cell Biology 72, 19–27. 10.1016/j.ceb.2021.04.003. [PubMed: 34015751]
9. Horne-Badovinac S, and Bilder D (2005). Mass transit: Epithelial morphogenesis in the Drosophila egg chamber. Developmental Dynamics 232, 559–574. 10.1002/dvdy.20286. [PubMed: 15704134]
10. Spradling AC (1993). Developmental Genetics of Oogenesis. In The Development of Drosophila melanogaster (Cold Spring Harbor Laboratory Press).
11. Viktorinová I, König T, Schlichting K, and Dahmann C (2009). The cadherin Fat2 is required for planar cell polarity in the Drosophila ovary. Development 136, 4123–4132. 10.1242/dev.039099. [PubMed: 19906848]
12. Markow TA, and O'Grady P (2006). Drosophila. A Guide to Species Identification and Use (Academic Press).
13. Crest J, oz AD-M, Chen D-Y, Fletcher DA, and Bilder D (2017). Organ sculpting by patterned extracellular matrix stiffness. Elife 6. 10.7554/eLife.24958.
14. Haigo SL, and Bilder D (2011). Global tissue revolutions in a morphogenetic movement controlling elongation. Science 331, 1071–1074. 10.1126/science.1199424. [PubMed: 21212324]
15. Bateman J, Reddy RS, Saito H, and Vactor DV (2001). The receptor tyrosine phosphatase Dlar and integrins organize actin filaments in the Drosophila follicular epithelium. Curr Biol 11, 1317–1327. [PubMed: 11553324]
16. Rust K, and Nystul T (2020). Signal transduction in the early Drosophila follicle stem cell lineage. Current Opinion in Insect Science 37, 39–48. 10.1016/j.cois.2019.11.005. [PubMed: 32087562]
17. Ellis SJ, Goult BT, Fairchild MJ, Harris NJ, Long J, Lobo P, Czerniecki S, Van Petegem F, Schock F, Peifer M, and Tanentzapf G (2013). Talin autoinhibition is required for morphogenesis. Curr Biol 23, 1825–1833. 10.1016/j.cub.2013.07.054. [PubMed: 24012314]
18. Grammont M, and Irvine KD (2002). Organizer activity of the polar cells during Drosophila oogenesis. Development 129, 5131–5140 [PubMed: 12399305]
19. Alégot H, Pouchin P, Bardot O, and Mirouse V (2018). Jak-Stat pathway induces Drosophila follicle elongation by a gradient of apical contractility. Elife 7. 10.7554/eLife.32943.
20. Xi R, McGregor JR, and Harrison DA (2003). A gradient of JAK pathway activity patterns the anterior-posterior axis of the follicular epithelium Developmental Cell 4, 167–177. [PubMed: 12586061]

21. Töpfer U, Guerra Santillán KY, Fischer-Friedrich E, and Dahmann C (2022). Distinct contributions of ECM proteins to basement membrane mechanical properties in Drosophila. Development 149. 10.1242/dev.200456.
22. Isabella AJ, and Horne-Badovinac S (2016). Rab10-Mediated Secretion Synergizes with Tissue Movement to Build a Polarized Basement Membrane Architecture for Organ Morphogenesis. Dev Cell 38, 47–60. 10.1016/j.devcel.2016.06.009. [PubMed: 27404358]
23. Cetera M, and Horne-Badovinac S (2015). Round and round gets you somewhere: collective cell migration and planar polarity in elongating Drosophila egg chambers. Curr Opin Genet Dev 32, 10–15. 10.1016/j.gde.2015.01.003. [PubMed: 25677931]
24. Bilder D, and Haigo, Saori L (2012). Expanding the Morphogenetic Repertoire: Perspectives from the Drosophila Egg. Developmental Cell 22, 12–23. 10.1016/j.devcel.2011.12.003. [PubMed: 22264728]
25. Chlasta J, Milani P, Runel G.l., Duteyrat J-L, Arias L, Lamiré L-A, Boudaoud A, and Grammont M (2017). Variations in basement membrane mechanics are linked to epithelial morphogenesis. Development 144, 4350–4362. 10.1242/dev.152652. [PubMed: 29038305]
26. Page-McCaw A (2008). Remodeling the model organism: Matrix metalloproteinase functions in invertebrates. Seminars in Cell & Developmental Biology 19, 14–23. 10.1016/j.semcdb.2007.06.004. [PubMed: 17702617]
27. Diwanji N, and Bergmann A (2020). Basement membrane damage by ROS- and JNK-mediated Mmp2 activation drives macrophage recruitment to overgrown tissue. Nature Communications 11. 10.1038/s41467-020-17399-8.
28. LaFever KS, Wang X, Page-McCaw P, Bhave G, and Page-McCaw A (2017). Both Drosophila matrix metalloproteinases have released and membrane-tethered forms but have different substrates. Sci Rep 7, 44560. 10.1038/srep44560. [PubMed: 28300207]
29. Valencia-Expósito A, Grosheva I, Míguez DG, González-Reyes A, and Martín-Bermudo MD (2016). Myosin light-chain phosphatase regulates basal actomyosin oscillations during morphogenesis. Nature Communications 7. 10.1038/ncomms10746.
30. Matsubayashi Y, Sanchez-Sanchez BJ, Marcotti S, Serna-Morales E, Dragu A, Diaz-de-la-Loza MD, Vizcay-Barrena G, Fleck RA, and Stramer BM (2020). Rapid Homeostatic Turnover of Embryonic ECM during Tissue Morphogenesis. Dev Cell. 10.1016/j.devcel.2020.06.005.
31. Keeley DP, Hastie E, Jayadev R, Kelley LC, Chi Q, Payne SG, Jeger JL, Hoffman BD, and Sherwood DR (2020). Comprehensive Endogenous Tagging of Basement Membrane Components Reveals Dynamic Movement within the Matrix Scaffolding. Developmental Cell 54, 60–74.e67. 10.1016/j.devcel.2020.05.022. [PubMed: 32585132]
32. Stevens LJ, Page-McCaw A, and Gonzalez-Gaitan M (2012). A secreted MMP is required for reepithelialization during wound healing. Molecular Biology of the Cell 23, 1068–1079. 10.1091/mbc.e11-09-0745. [PubMed: 22262460]
33. Loza M.C.D. d.l., Díaz-Torres A, Zurita F, Rosales-Nieves AE, Moeendarbary E, Franze K, Martín-Bermudo MD, and González-Reyes A (2017). Laminin Levels Regulate Tissue Migration and Anterior-Posterior Polarity during Egg Morphogenesis in Drosophila. Cell Rep 20, 211–223. 10.1016/j.celrep.2017.06.031. [PubMed: 28683315]
34. Ross TD, Coon BG, Yun S, Baeyens N, Tanaka K, Ouyang M, and Schwartz MA (2013). Integrins in mechanotransduction. Current Opinion in Cell Biology 25, 613–618. 10.1016/j.ceb.2013.05.006. [PubMed: 23797029]
35. Nukuda A, Sasaki C, Ishihara S, Mizutani T, Nakamura K, Ayabe T, Kawabata K, and Haga H (2015). Stiff substrates increase YAP-signaling-mediated matrix metalloproteinase-7 expression. Oncogenesis 4, e165–e165. 10.1038/oncsis.2015.24. [PubMed: 26344692]
36. Haage A, and Schneider IC (2014). Cellular contractility and extracellular matrix stiffness regulate matrix metalloproteinase activity in pancreatic cancer cells. The FASEB Journal 28, 3589–3599. 10.1096/fj.13-245613. [PubMed: 24784579]
37. Rider L, Oladimeji P, and Diakonova M (2013). PAK1 Regulates Breast Cancer Cell Invasion through Secretion of Matrix Metalloproteinases in Response to Prolactin and Three-Dimensional Collagen IV. Molecular Endocrinology 27, 1048–1064. 10.1210/me.2012-1322. [PubMed: 23744893]

38. Favreau AJ, Vary CPH, Brooks PC, and Sathyanarayana P (2014). Cryptic collagen IV promotes cell migration and adhesion in myeloid leukemia. Cancer Medicine 3, 265–272. 10.1002/cam4.203. [PubMed: 24519883]

39. Zhang K, Corsa CA, Ponik SM, Prior JL, Piwnica-Worms D, Eliceiri KW, Keely PJ, and Longmore GD (2013). The collagen receptor discoidin domain receptor 2 stabilizes SNAIL1 to facilitate breast cancer metastasis. Nature Cell Biology 15, 677–687. 10.1038/ncb2743. [PubMed: 23644467]

40. Biggins JD, Thompson JE, and Birkhead TR (2018). Accurately quantifying the shape of birds' eggs. Ecology and Evolution 8, 9728–9738. 10.1002/ece3.4412. [PubMed: 30386570]

41. Stoddard MC, Yong EH, Akkaynak D, Sheard C, Tobias JA, and Mahadevan L (2017). Avian egg shape: Form, function, and evolution. Science 356, 1249–1254. DOI: 10.1126/science.aaj1945. [PubMed: 28642430]

42. Wachsmuth M (2014). Molecular diffusion and binding analyzed with FRAP. Protoplasma 251, 373–382. 10.1007/s00709-013-0604-x. [PubMed: 24390250]

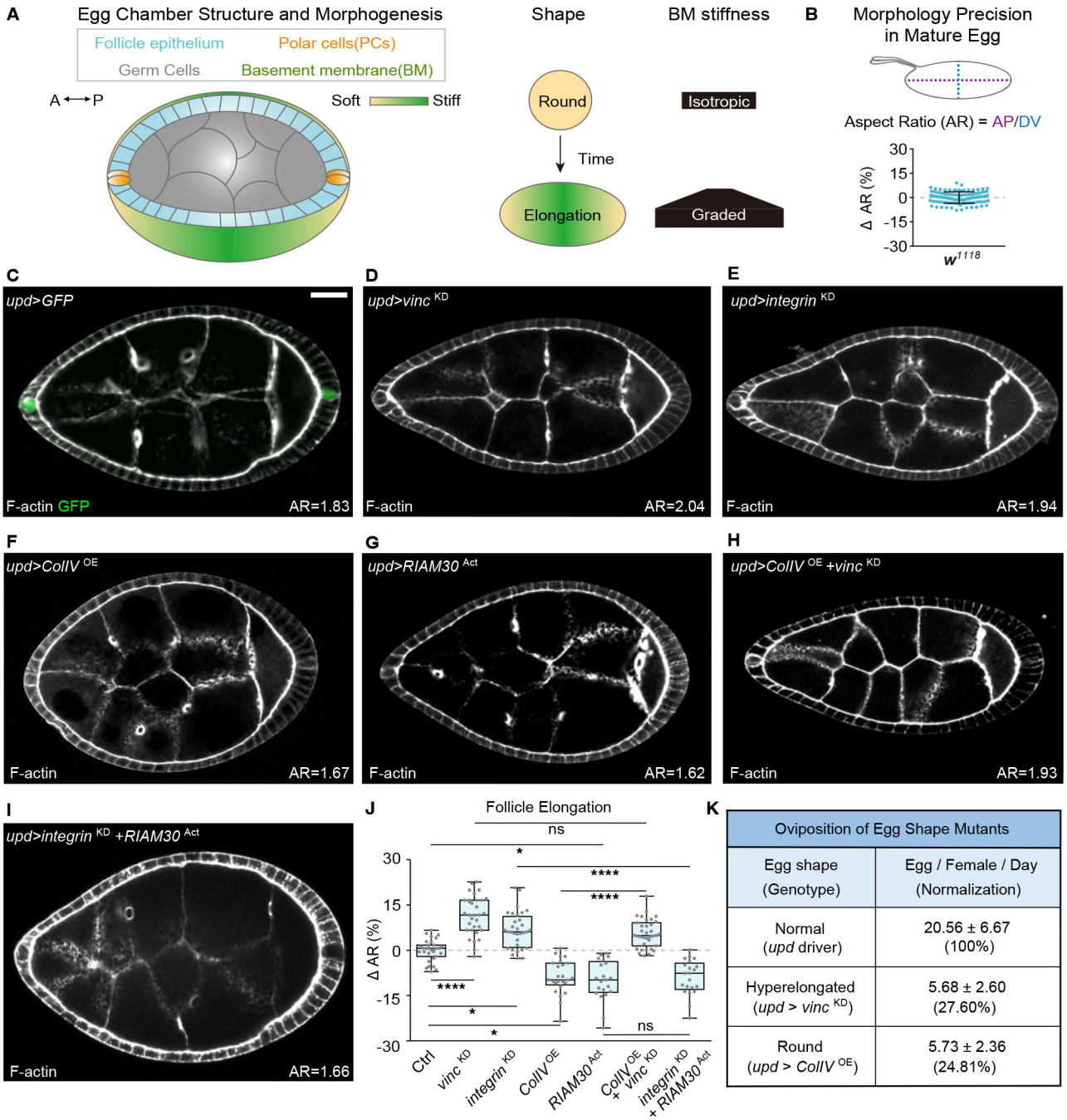

K

Oviposition of Egg Shape Mutants	
Egg shape (Genotype)	Egg / Female / Day (Normalization)
Normal (*upd* driver)	20.56 ± 6.67 (100%)
Hyperelongated (*upd* > *vinc* ^{KD})	5.68 ± 2.60 (27.60%)
Round (*upd* > *ColIV* ^{OE})	5.73 ± 2.36 (24.81%)

Figure 1. Polar cells direct tissue elongation through BM-responsive focal adhesion signaling.

(**A**) Overview of follicle elongation, showing cell types involved, along with mechanical patterning of the ECM that drives morphogenesis.

(**B**) Variation of aspect ratio (AR: AP/DV length) in wild-type eggs (w^{1118}, n=108). Bar graph is mean ± standard deviation (0 ± 3.55%) subtracted to mean.

(**C**) Location of PCs, as displayed by *upd*-GAL4-driven GFP (n=19). F-actin marks follicle morphology. Mean AR is indicated in bottom right from this panel onward. Scale bars hereafter are 20 μm unless otherwise indicated.

(**D**-**G**) PC-specific knockdown (KD) of focal adhesion components Vinc (**D**, n=32) or Integrin (**E**, n=32) induces follicle hyperelongation, while overexpression (OE) of ColIV (**F**, n=25) or RIAM30^{Act} (**G**, n=21) causes hypoelongation.

(**H**) Overexpression of ColIV with simultaneous depletion of Vinc (n=35) shows that Vinc acts downstream of ColIV in follicle shaping.

(I) Overexpression of RIAM30^{Act} in PCs reverses the hyperelongation phenotype of Integrin depletion (n=32).

(**J**) Quantitation of follicle elongation in Ctrl (**C**, *upd* driver, n=31) and **D**-**I**. Statistics are shown in box and whiskers (Min to Max) plot, with comparisons performed using ANOVA with Dunnett's multiple comparisons. *P < 0.05, **P < 0.01, ***P < 0.001, ****P < 0.0001, and n.s., not significant (P > 0.05).

(**K**) Oviposition rates for eggs with elongation phenotypes generated by PC manipulation. n for *upd*, *upd>vinc*^{KD}, and *upd>ColIV*^{OE} = 2056, 227, and 344 respectively.

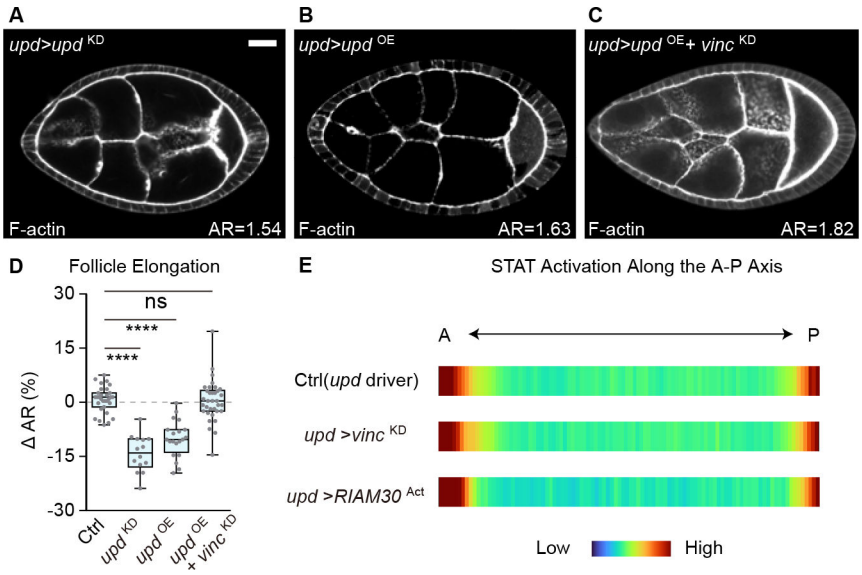

Figure 2. Focal adhesion signaling in the PCs functions independent of Upd.

(**A-B**) Round follicles are induced by either depleting (**A**, n=14) or overexpressing (**B**, n=19) Upd from PCs.

(**C**) PC-specific Upd overexpression combined with Vinc depletion generates follicles with elongation phenotypes intermediate between either single manipulation (n=33).

(**D**) Quantitation of follicle elongation in **A**-**C**. Statistics used ANOVA with Dunnett's multiple comparisons.

(**E**) Quantitation of STAT activation along the A-P axis (shown as averaged heat map, see also Figure S2H–K) reveals no difference between control follicles and those with PC-specific manipulation of focal adhesion components.

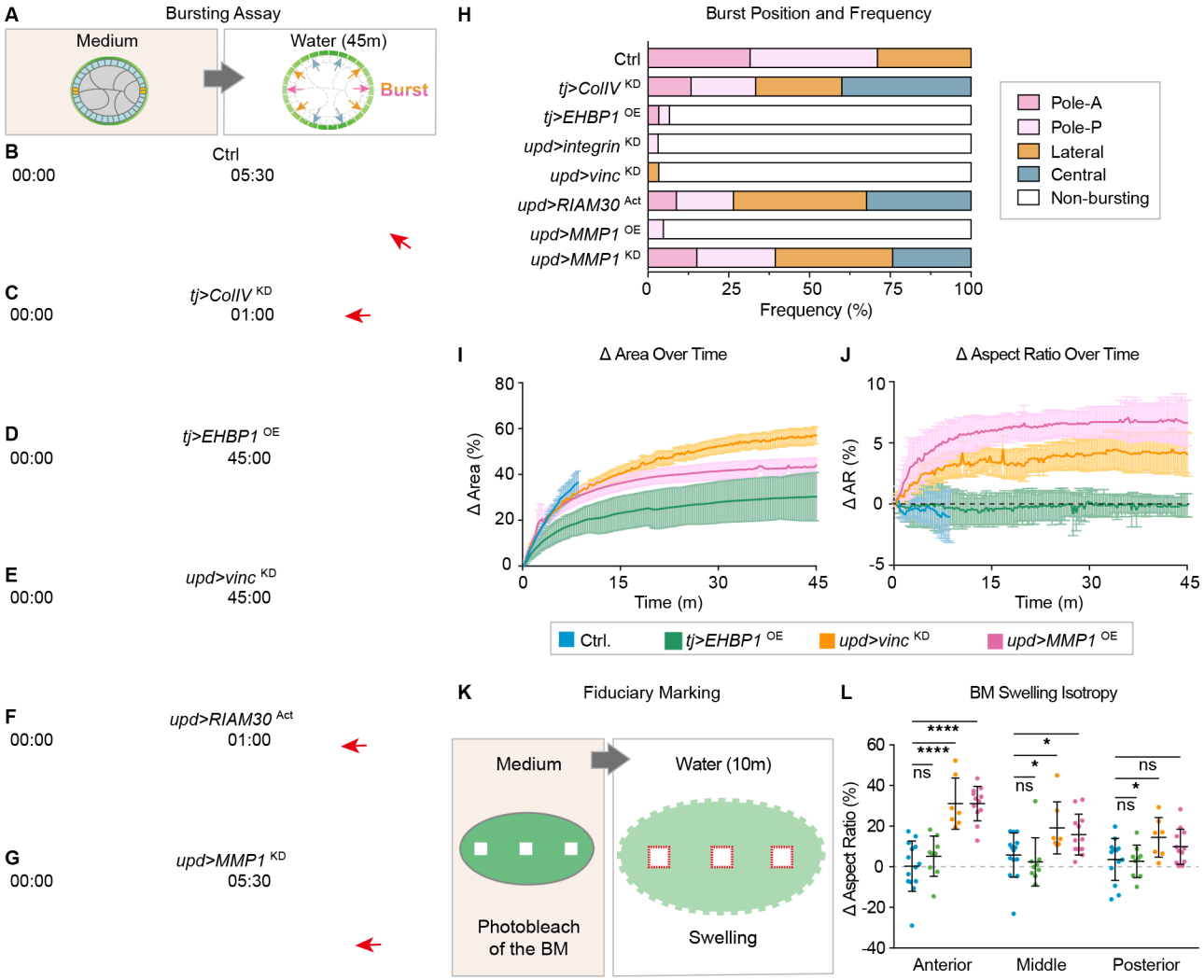

Figure 3. Focal adhesion signaling in PCs tunes follicle mechanical properties.

(**A**) Illustration of hypotonic bursting assay to assess BM mechanical properties. Red (poles) and orange (lateral) arrows indicate the regions that preferentially burst due to softer BM in normal follicle. Blue arrows indicate the central part of the follicle that does not burst normally.

(**B-G**) Bursting assays on control follicles (**B**), follicles with epithelium-wide BM manipulation (**C**, softer BM, *tj>ColIV*^{KD}; **D**, stiffer BM, *tj>EHBP1*^{OE}), and follicles with PC-specific manipulation (**E**, *upd>vinc*^{KD}; **F**, *upd>RIAM30*^{Act}; **G**, *upd>MMP1*^{KD}). Time in hypotonic solution is indicated in each frame as minutes:seconds. Images in right panels show time of follicle bursting (red arrows) or at the end of experiment for non-bursting follicles (45:00). See Video S1.

(**H**) Quantitation of burst positions and frequency from **B-G**. n values are 38, 15, 30, 32, 30, 34,21, and 33 respectively.

I-J) Quantitation of follicle expansion kinetics during osmotic swelling of control and hyperelongated genotypes. Data shown are mean ± standard deviation. Genotype-color codings are consistent in I,J, and L.

(K) Diagram showing fiduciary photobleaching of ColIV-GFP squares in anterior, central and posterior positions of follicles, followed by transfer to ddH_20 to induce osmotic swelling.

(L) Quantitation of change of photobleached squares following swelling. Squares in control (n=14) follicles or hyperelongated EHBP1-overexpressing follicles (n=9) show no change in aspect ratio regardless of position along AP axis, whereas squares in the anterior of follicles with PC FA depletion (n=7) or MMP1 overexpression (n=12) show greater extension along the AP axis, making rectangles. Smaller but significant extension is seen with these genotypes in squares bleached in the central follicle, as well as in the posterior for PC FA depletion. Statistics used multiple-t-tests.

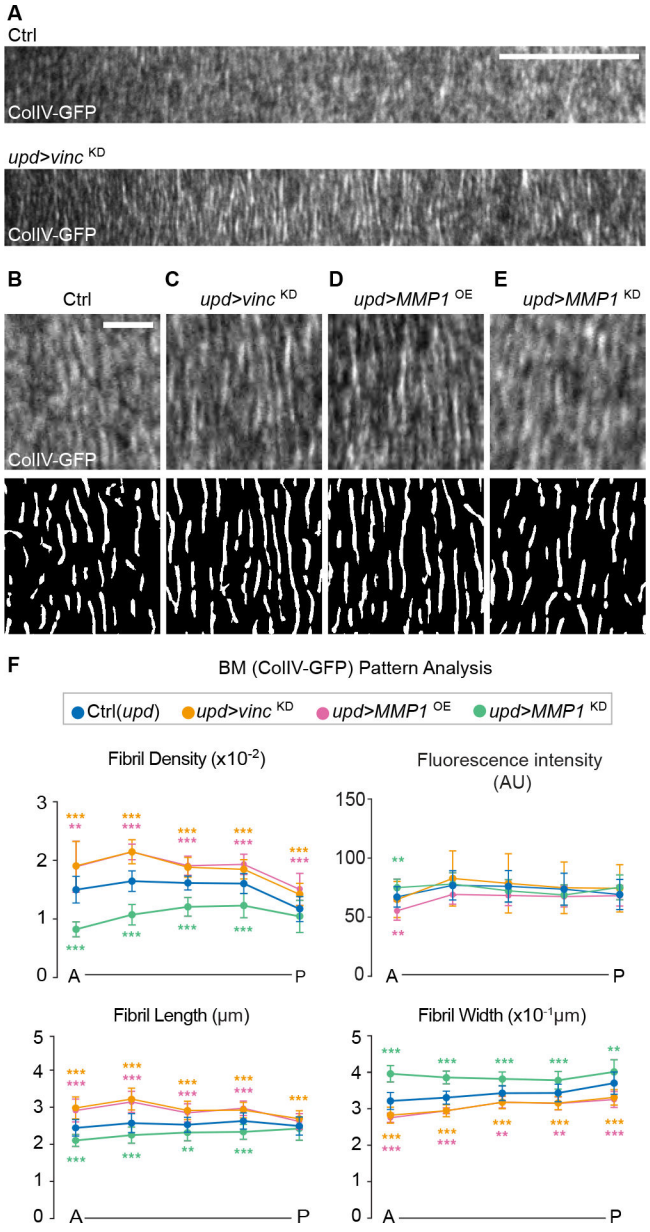

Figure 4. Control of BM patterning by PC focal adhesion signaling.

(**A**) ColIV-GFP patterns from the anterior regions of control (n=26) and hyperelongated follicles (*upd*> *vinc*^{KD}, n=37).

(**B-E**) ColIV-GFP (upper) and fibril map (fibrils in white, see Methods) in control (**B)** and PC-specific manipulations (**C**, *upd*>*vinc*^{KD}; **D,** *upd*>*MMP1*^{OE}, n=9; **E**, *upd*>*MMP1*^{KD}, n=16). Scale bar= 5 µm.

(**F**) Quantitation of ColIV-GFP fibril density, length and width along the A-P axis from **B-E**. Statistics used multiple-t-tests.

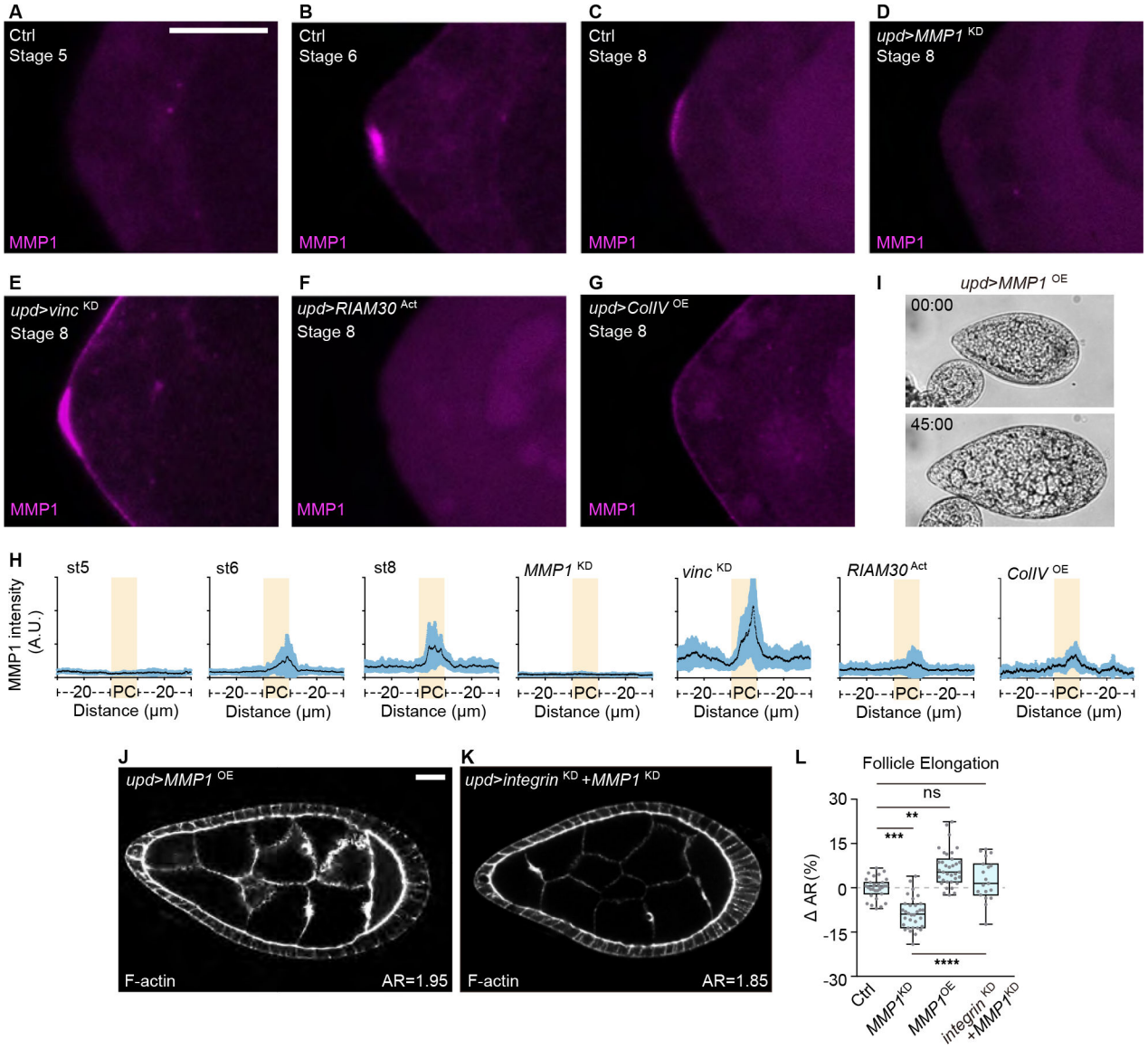

Figure 5. Focal adhesion-regulated MMP1 from PCs promotes tissue elongation.

(**A-G**) Images of anterior pole of developing follicles in ice preps. In control, MMP1 can be detected from stage 6 (**A**, stage 5, n=7; **B**, stage 6, n=15; **C**, stage 8, n=20). Staining of MMP1 is absent upon MMP1 depletion in the PCs (**D,** n=6). PC focal adhesion depletion leads to increased levels (**E**, n=13), while MMP1 in the PCs is reduced upon focal adhesion activation (**F**, n=9) or ColIV overexpression (**G,** n=16). Scale bars = 10 μm.

(**H**) Quantitation of MMP1 signal intensity along the follicle anterior pole, centered around the PCs (highlighted in yellow) for a total of 50 μm.

(**I-J**) Overexpressing MMP1 in PCs results in follicles that resist bursting upon osmotic shock (**I,** quantitation in Figure 3H–J, n=21) and is sufficient to drive hyperelongation (**J**).

(**K**) Co-depletion of MMP1 attenuates follicle hyperelongation induced by Integrin depletion from PCs.

(**L**) Quantitation of follicle elongation from Ctrl (*upd* driver, n=31), **D** (n=32), **I** (n=35), and **J** (n=19). Statistics used ANOVA with Dunnett's multiple comparisons.

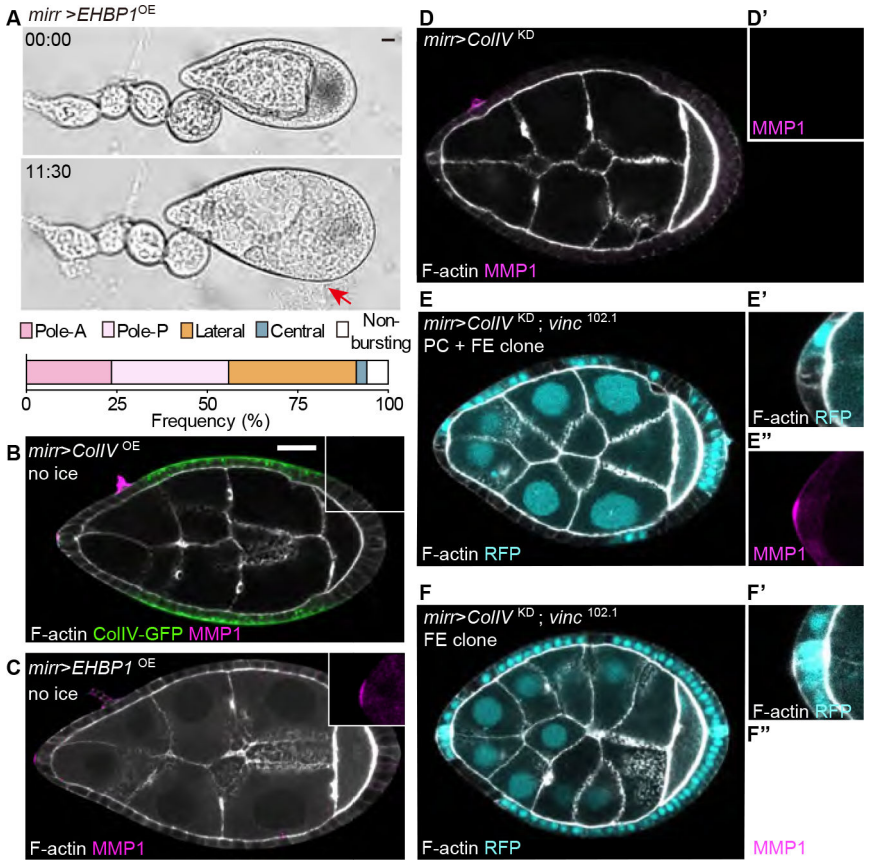

Figure 6. PCs sense and react to non-local BM changes through focal adhesion signaling.

(**A**) Bursting assay of BM fibril increase in the central follicle epithelium (*mirr>EHBP1*^{OE}, n=34). Red arrow indicates burst position.

(**B-C**) Overexpressing ColIV (**B**, green, n=20) or EHBP1 (**C**, n=25) in the central follicle causes anterior PCs to upregulate MMP1 (magnified in insets). Non-ice preps.

(D) Depleting ColIV in the central follicle causes anterior PCs to downregulate MMP1 (n=6). Ice prep.

(**E-F**) MMP1 expression when central follicle ColIV depletion is combined with blocking focal adhesion signaling (*vinc* mutant clones, not expressing RFP) in either PCs and epithelium (**E**, n=11), or in epithelium alone (**F**, n= 15). Ice preps.

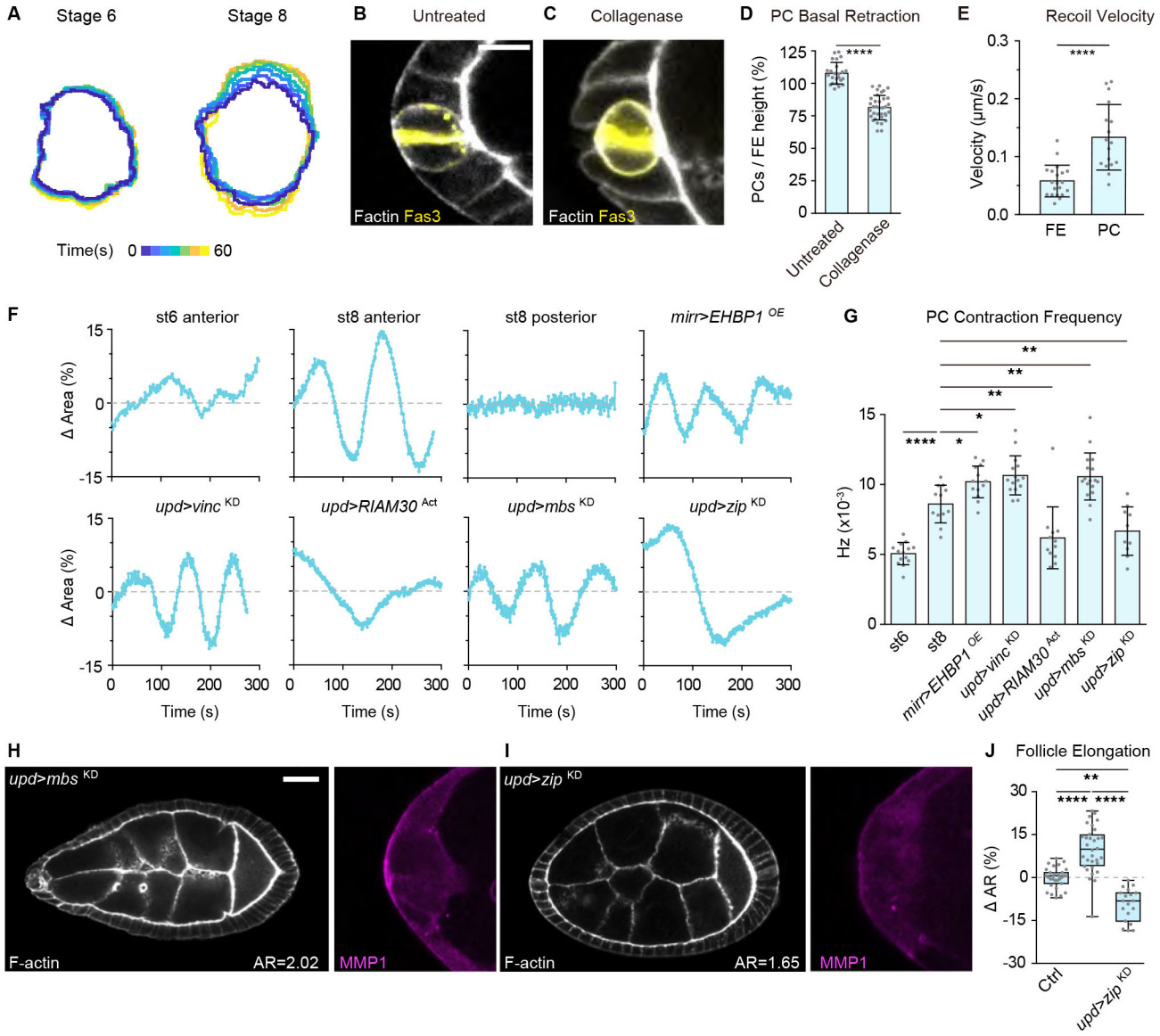

Figure 7. PCs tug on the BM for mechanical sensing.

(**A**) Dynamic contractility of anterior PCs in live follicles. Outlines of Fas3-GFP signals are overlayed and color-coded according to time (stage 6, n=14; stage 8, n=12, Video S4).

(**B**-**C**) PCs (labeled by Fas3 staining, yellow) in untreated (**B**, n=24) or collagenase-treated (**C**, n=35) follicles. Scale bars: 10 μm.

(**D**) Quantitation of PC basal retraction, normalized to the immediate neighboring follicle epithelium. Statistics used unpaired Mann-Whitney test.

(E) Recoil velocity of lateral plasma membranes following cortical severing with a 2-photon laser. Recoil is higher in PCs (n=17) then follicle epithelial cells (n=20). Statistics used unpaired Mann-Whitney test.

(**F**) Single PC contractility dynamics over time. PCs in control (anterior: stage 6, n=14; stage 8 n=12; posterior: stage 8 n=12) and manipulated (central stiffening: *mirr>EHBP1*^{OE}, n=14;

PC mutants: *upd>vinc*^{KD}, n=15; *upd>RIAM30*^{Act}, n=12; *upd>mbs*^{KD}, n=17; *upd>zip*^{KD}, n=10, see Video S5) stage 8 follicles.

(**G**) Quantitation of PC contraction frequency in control and manipulated follicles. Statistics used KS (Kolmogorov-Smirnov) test.

(**H-I**) Increasing PC contractility (**H**, *upd>mbs*^{KD}, n=31) leads to follicle hyperelongation and MMP1 upregulation, while decreasing PC contractilty (**I**, *upd>zip*^{KD}, n=23) has the opposite effect.

(J) Quantitation of aspect ratios in H, I. Statistics used ANOVA with Dunnett's multiple comparisons.

Key resources table

REAGENT or RESOURCE	SOURCE	IDENTIFIER
Antibodies		
Rabbit anti-β-gal; Dilution 1:1000	Abcam	RRID: AB_305327
Mouse anti-Eyes Absent; Dilution 1:100	Hybridoma Bank	RRID: AB_528232
Mouse anti-Fas3; Dilution 1:100	Hybridoma Bank	RRID: AB_528238
Mouse anti-GFP; Dilution 1:50	ThermoFisher	RRID: AB_2313858
Rabbit anti-GFP; Dilution 1:500	Torrey Pines	RRID: AB_2313770
Mouse anti-MMP1; Dilution 1:100	Hybridoma Bank	RRID: AB_579780
Mouse anti-MMP1; Dilution 1:100	Hybridoma Bank	RRID: AB_579781
Mouse anti-MMP1; Dilution 1:100	Hybridoma Bank	RRID: AB_579779
Alexa Fluor 488 anti-mouse; Dilution 1:200	Invitrogen	RRID: AB_2534069
Alexa Fluor 488 anti-rabbit; Dilution 1:200	Invitrogen	RRID: AB_143165
Alexa Fluor 647 anti-mouse; Dilution 1:100	Invitrogen	RRID: AB_162542
Alexa Fluor 647 anti-rabbit; Dilution 1:100	Invitrogen	RRID: AB_2535812
Alexa Fluor-647 anti-GFP Nanobody; Dilution 1:2000	ChromoTek	RRID: AB_2827575
Chemicals, peptides, and recombinant proteins		
Paraformaldehyde; 4% (v/v)	Electron Microscopy Science	15710 (EM Grade)
TRITC-Phalloidin; Dilution 1:200	Sigma	P1951
Alexa Fluor 647-Phalloidin; Dilution 1:50	Invitrogen	A22287
CellMask Deep Red; Dilution 1:1000	Invitrogen	C10046
DAPI; Dilution 1:2000	ThermoFisher	D1306
Normal goat serum; 5% (v/v)	Gibco	PCN5000
Collagenase; 1000 U/mL	Worthington	LS005273
Low melt agarose; 1% (w/v)	Bio-RAD	161–3113
Schneider's Drosophila Medium	Gibco	21720024
Poly-D lysine: 100 μg/mL	Millipore	633307
SlowFade Antifade solution	Invitrogen	S2828
Experimental models: Organisms/strains		
D. melanogaster: w^{1118}	BDSC	5905
D. melanogaster: tj-GAL4, tub-GAL80^{TS}/CyO	Kyoto Stock Center	104055
D. melanogaster: upd-GAL4; +; tub-GAL80^{TS},UAS-Dicer2/TM3	BDSC	26796
D. melanogaster: tub-GAL80^{TS}; mirr-GAL4/TM3, Sb, twi-GFP	Anne-Marie Pret, French National Centre for Scientific Research	PMID23222440
D. melanogaster: hs-FLP^{122}; +; Act5c>CD2>GAL4, UAS-RFP	BDSC	30558
D. melanogaster: UAS-nls-GFP	BDSC	4776
D. melanogaster: w; UAS-Red-Stinger,UAS-FLP, Ubi-p63E(FRT.STOP)-Stinger*	BDSC	28281; PMID19633663
D. melanogaster: w^{1118}; 10XStat92E-dGFP/CyO	BDSC	26199; PMID17008134
D. melanogaster: w^{1118}; 10XStat92E-GFP/TM6C	BDSC	26198; PMID17008134

REAGENT or RESOURCE	SOURCE	IDENTIFIER
D. melanogaster: Vinc-RFP(II)	Nicholas H Brown, University of Cambridge	PMID25754646
D. melanogaster: w^{1118}; $Ilk^{ZCL3111}$-GFP	BDSC	6831; PMID14681446
D. melanogaster: $neur^{A101}$-lacZ /TM3, ryRK Sb^{1} Ser^{1}	BDSC	4369; PMID1879352
D. melanogaster: $vkg^{CC00791}$-GFP	Allan C. Spradling, Carnegie Institution for Science	PMID17194782
D. melanogaster: w^{1118}; His2AvGFP-S65T	BDSC	5941
D. melanogaster: $Indy^{CC00377}$-GFP	Allan C. Spradling, Carnegie Institution for Science	PMID17194782
D. melanogaster: w; $Fas3^{G00258}$ -GFP*	BDSC	50841; PMID14681446
D. melanogaster: $Vinc^{102.1}$	Nicholas H Brown, University of Cambridge	PMID25754646
D. melanogaster: egl^{WU50}/egl^{RC12}	Trudi Schupbach, Princeton University	PMID28306055
D. melanogaster: yki^{B5}	Doujia Pan, Southwestern Medical Center	PMID16096061
D. melanogaster: y^{1},sc,v^{1},sev^{21}; UAS-GFP $RNAi^{VALIUM20}$*	BDSC	41553
D. melanogaster: y^{1},v^{1}; UAS-vinc RNAi ^{JF01985}	BDSC	25965;455299
D. melanogaster: y^{1},sc,v^{1}; UAS-vinc RNAi ^{HMS02356}*	BDSC	455299
D. melanogaster: y^{1},sc,v^{1}; UAS-ilk RNAi ^{GL00288}*	BDSC	35374; PMID24046451
D. melanogaster: y^{1},sc,v^{1}; UAS-ilk RNAi ^{HMS04509}*	BDSC	47308; PMID29440263
D. melanogaster: y^{1},v^{1}; UAS-integrin RNAi ^{HMS00043}	BDSC	33642; PMID34980203
D. melanogaster: w^{1118}; UAS-integrin RNAi ^{GD15002}	VDRC	30619; PMID25053436
D. melanogaster: UAS-cg25c-GFP/CyO; UAS-vkg-GFP/TM6c	Stéphane Noselli, University of Nice	PMID26456819
D. melanogaster: UAS-vkg $RNAi^{v106812}$; UAS-cg25c $RNAi^{HMC03010}$	VDRC; BDSC	v106812; 44520
D. melanogaster: UAS-mCherry-RIAM30-$RAP1^{CAAX}$	Guy Tanentzapf, University of British Columbia	PMID24012314
D. melanogaster: y^{1},v^{1}; UAS-Upd RNAi ^{JF03149}	BDSC	28722; PMID23021220
D. melanogaster: UAS-Upd(II)	Anne Classen, University of Freiburg	PMID19749759
D. melanogaster: y^{1}, w; UAS-FLAG-$Ehbp1^{VK00033}$*	BDSC	67146
D. melanogaster: y^{1},v^{1}; UAS-MMP1 $RNAi^{JF01336}$	BDSC	31489; PMID30982664
D. melanogaster: UAS-Mmp1RNAi ^{KK108894}	VDRC	101505; PMID25356918
D. melanogaster: w; UAS-Mmp1.f1*	BDSC	58700; PMID32686670
D. melanogaster: w; UAS-Mmp1.f1*	BDSC	58701; PMID32686670
D. melanogaster: w; UAS-Mmp2.P*	BDSC	58705; PMID32686670
D. melanogaster: w; UAS-Mmp2.P*	BDSC	58706; PMID32686670
D. melanogaster: y^{1},v^{1}; UAS-mbs $RNAi^{GL01207}$	BDSC	41625; PMID32916115
D. melanogaster: UAS-zip $RNAi^{GD1566}$	VDRC	v7819; PMID20498300
D. melanogaster: y^{1},v^{1}; UAS-α-catenin $RNAi^{HMS00317}$	BDSC	33430; PMID30659113
D. melanogaster: y^{1},v^{1}; UAS-yki $RNAi^{HMS00041}$	BDSC	34067; PMID29440303

REAGENT or RESOURCE	SOURCE	IDENTIFIER
D. melanogaster: UAS-vkg RNAi^{v106812}; UAS-cg25c RNAi^{HMC03010}	VDRC; BDSC	v106812; 44520
Software and algorithms		
Prism 6.0	GraphPad	www.graphpad.com
Fiji 2.3.9/1.53p	ImageJ	http://fiji.sc/
Zen (black edition)	Zeiss	https://www.zeiss.com
Illustrator 22.0.1	Adobe	www.adobe.com/uk/products/illustrator.html
Imaris 9.3.1	Bitplane	https://imaris.oxinst.com/
Matlab R2021a	MathWorks	https://www.mathworks.com/